Chemical Engineering Journal 526 (2025) 170994

Contents lists available at ScienceDirect

Chemical Engineering Journal

journal homepage: www.elsevier.com/locate/cej

Integrated design, scale-up, and surrogate-based optimization of PSA systems for hydrogen purification from ammonia decomposition

Bahare Abdoos, Almerinda Di Benedetto, Danilo Russo *

Department of Chemical Engineering, Materials, and Industrial Production, University of Naples Federico II, P.le V. Tecchio 80, 80125, Naples, Italy

ARTICLE INFO

Keywords:
Pressure swing adsorption
Multi-objective optimization
Surrogate modeling
Hydrogen purification
Ammonia decomposition
Gas separation

ABSTRACT

Green hydrogen production from liquid organic hydrogen carriers such as ammonia is a key pathway toward decarbonization and net-zero emissions. However, hydrogen derived via ammonia decomposition must be further purified to meet stringent requirements of some applications, including adoption in fuel cells. This study presents a framework for the design, modeling, and multi-objective optimization of a purification unit based on pressure swing adsorption (PSA). An adsorption model was developed and validated against experimental isotherms and breakthrough data. The validated model was then scaled to industrial conditions to serve as a base-case simulation. A detailed sensitivity analysis was conducted to evaluate the impact of key operational and design variables—including bed length, diameter, pressure, temperature, and flow rate—on four critical performance indicators: hydrogen purity, recovery, productivity, and specific energy consumption (SEC). A surrogate model was trained using high-fidelity simulation data and integrated with the Non-dominated Sorting Genetic Algorithm II (NSGA-II) to generate Pareto-optimal solutions. The surrogate model's predictions were successfully validated against full-order simulations. The optimization results revealed three distinct operating regions, each representing a trade-off between purity, recovery, and energy efficiency. Notably, the proposed design achieves up to 99.99 % hydrogen purity with a recovery of 77.4 %, and SEC values as low as 5.19 MJ/kg H_2. Compared to baseline configurations, the recommended design achieves improvements of 2.78 % in hydrogen purity and 11.11 % in energy efficiency, offering a promising and scalable strategy for ammonia-based hydrogen purification systems. The economic assessment, based on technical performance, estimated the projected cost of purifying hydrogen to 99.99 % concentration using an industrial-scale PSA unit fed by ammonia decomposition. These evaluations suggest a pathway to produce high-purity hydrogen supporting its integration into energy markets.

List of symbols

C_{pa}	Adsorbed phase heat capacity (kJ/kmol·K)
C_{ps}	Solid heat capacity(MJ/kg·K)
$C_{g,i}$	Concentration of component in gas phase (kmol/m^3)
C_T	Gas phase total concentration (kmol/m^3)
C_{vg}	Specific gas heat capacity at constant volume(MJ/kmol·K)
D	Bed diameter (m)
d_p	Particle diameter(m)
D_b	Internal diameter of adsorbent layer (m)
D_m	Molecular diffusion coefficient (m^2/s)
Ez	Axial dispersion coefficient (m^2/s)
F	Feed flow rate
H_b	Height of adsorbent layer (m)
HTC	Heat transfer coefficient (MW/m^2·K)
L	bed length (m)
Kga	Effective heat conductivity
MTC	Mass transfer coefficient (1/s)
Mw	Molecular weight (kg/kmol)
P_{ads}	Adsorption Pressure (bar)
RE	Reynolds (−)
r_p	Particle radius (m)
T	Feed temperature
Tg	Gas phase temperature (°C)
Ug	Gas phase superficial velocity (m/s)
Q	Solid loading (kmol/kg)
Q^*	Solid equilibrium loading (kmol/kg)
ρ_b	Bulk density (kg/m^3)
ρ_p	Adsorbent density (g/m^3)
ρ_g	Gas phase density (kmol/m^3)

* Corresponding author.
E-mail address: danilo.russo3@unina.it (D. Russo).

https://doi.org/10.1016/j.cej.2025.170994
Received 16 July 2025; Received in revised form 14 October 2025; Accepted 16 November 2025
Available online 19 November 2025

(*continued*)

P_p	Particle density (kg/m^3)
ψ	Shape factor (−)
ε_p	Intraparticle voidage ($m^3_{pore}/m^3_{particle}$)
ε_b	Interparticle voidage (m^3_{void}/m^3_{bed})
ε_t	Total bed voidage (m^3_{void+} m^3_{pore})/ m^3_{bed}
ΔH	Heat of adsorption (kJ/mol)
μ	Viscosity of the fluid (N·s/m^2)
τ	residence time (s)

1. Introduction

The development of environmentally sustainable, economically viable, and efficient alternatives to fossil fuels is a critical objective for addressing the increasing global energy demand while mitigating climate change [1]. In this context, hydrogen has emerged as a promising energy vector due to its high energy density and clean combustion profile [2]. However, the widespread adoption of hydrogen is significantly constrained by scientific and technological challenges, particularly regarding its safe, efficient, and cost-effective storage and distribution [3]. Among the proposed solutions, liquid ammonia (NH_3) has gained considerable attention as a hydrogen carrier [4]. Ammonia offers several advantages, including a high hydrogen content and favorable storage characteristics. Specifically, it exhibits one of the highest volumetric (121 kg H_2 m^{-3} at 10 bar) and gravimetric (17.8 wt %) hydrogen densities. It can also be liquefied under relatively mild conditions (below 10 bar at ambient temperature) [5]. Furthermore, ammonia benefits from an established industrial infrastructure and well-defined handling protocols [6].

The catalytic decomposition of green ammonia represents a viable pathway for CO_2-free hydrogen release, following the reaction:

$$2NH_3 \leftrightarrow N_2 + 3H_2 \ (\Delta H = +46.2\ KJ/mol_{NH3})$$

Under optimized catalytic conditions, this process yields a gas mixture theoretically composed of 25 % nitrogen (N_2) and 75 % hydrogen (H_2), with ammonia present at trace levels. Previous studies have shown that commercially available adsorbents, such as Ammosorb (manufactured by Nucor, Inc.), can reduce ammonia levels to ppb after cracking, which is compatible with most applications [7]. Numerous studies have investigated various transition-metal-based catalysts, with particular emphasis on Ru-supported systems on basic and electron-conductive supports, aiming to maximize ammonia conversion, selectivity, and hydrogen purity. [8,9] A key challenge in this approach lies in the separation of hydrogen from nitrogen. Nitrogen, although less harmful to fuel cells than carbon monoxide or carbon dioxide, reduces hydrogen purity and contributes to increased resistance and long-term degradation in proton exchange membrane fuel cells (PEMFCs). High-temperature PEM fuel cells (HT-PEMFCs), particularly those based on polybenzimidazole (PBI), are more tolerant to such impurities. However, the presence of nitrogen (e.g., 20 vol%) has been shown to significantly increase both kinetic and proton transfer resistance, ultimately impairing fuel cell efficiency, especially for low-temperature fuel cells. This underscores the importance of high-purity hydrogen streams in energy applications [10].

Pressure Swing Adsorption (PSA) has emerged as a promising technology for hydrogen purification, offering advantages such as compact design, low energy requirements, reduced capital investment, operational safety and simplicity, and high purity levels (up to 99.99 %) [11,12]. PSA operates based on differences in gas adsorption behavior—either equilibrium or kinetic—on solid adsorbents subjected to cyclic pressure changes. The process, originally developed by Skarstrom, typically involves four main steps: adsorption, depressurization, purge, and repressurization. Its versatility allows adaptation through various configurations, step durations, adsorbent types, and system scales [13]. The versatility of PSA technology lies in its adaptability to a wide range of operational parameters, including the selection of adsorbent materials, step durations, cycle configurations, operating pressures, column dimensions, and the use of single- or multi-bed systems [11]. Ahn et al. conducted both experimental and theoretical investigations on layered two-bed and four-bed PSA systems for hydrogen recovery from coke oven gas, utilizing activated carbon and 5 A zeolite as adsorbents. Their four-bed configuration, with nitrogen as the main impurity, achieved hydrogen purities between 96 % and 99.5 %, with recovery rates ranging from 71 % to 85 % [14]. Similarly, Moon et al. [15] developed a hydrogen PSA process integrated with gasification-based syngas production, studying both experimentally and theoretically two-bed and multi-layer configurations. Using activated carbon and activated carbon/zeolite LiX, they achieved hydrogen purity of 99.77 %–99.95 % with a recovery rates between 73.30 % and 77.64 % in a two-bed system operating at 25–35 bar. A four-layered bed configuration at 35 bar yielded hydrogen with a purity of 99.97 % and a recovery of 79 %. As plant scale increases, the development of empirically validated performance enhancement strategies becomes increasingly complex and expensive. In this context, small-scale PSA or TSA systems serve as indispensable tools for both adsorbent manufacturers and users. Small adsorbers allow rapid evaluation of adsorbent quality with minimal material usage, and they facilite the exploration of optimal cycle configurations and plant designs at reduced capital costs. Furthermore, experimental data obtained from these small-scale systems can be effectively used to inform process modeling and support the design and optimization of full-scale units. [16]

Recent study [17] evaluated various PSA and membrane-based configurations for H_2/N_2, particularly in the context of hydrogen recovery from ammonia decomposition. One such study investigated eight setups using Zeolite 13X as the adsorbent, identifying a hybrid PSA–membrane system as the most efficient. This configuration achieved >95 % hydrogen recovery and 85.4 % system efficiency, significantly outperforming the PSA-only system (66 % recovery, 59.1 % efficiency).. Additionally, the PSA–membrane configuration yielded the lowest levelized cost of hydrogen (LCOH) at 4.31 €/kg—22 % lower than the PSA-only setup. However, the high cost of palladium membranes limits the economic feasibility of membrane-only systems. As the analysis was conducted at small scale (~300 Nm^3/h), further validation is required for industrial deployment. Nonetheless, the results underscore the promise of NH_3-based hydrogen production as a viable alternative to methane steam reforming with carbon capture, provided further cost reductions are achieved. Parallel efforts have explored advanced adsorbents, particularly Metal–Organic Frameworks (MOFs), owing to their high surface area and structural tunability. A high-throughput screening (HTS) of 12,020 MOFs identified promising candidates for H_2/N_2 separation, with RAVXIX emerging as a top performer in GCMC-based PSA simulations. However, limited thermal stability—disqualifying 7 of the top 20 MOFs—remains a major barrier to practical application. These drawbacks, along with high regeneration energy and cost, currently limit MOFs' feasibility, reinforcing the role of zeolites as the preferred industrial adsorbents due to their robustness, affordability, and proven performance. [18]

On the modeling side, simulating and optimizing PSA processes remains computationally intensive due to the stiffness of coupled partial differential equations and sharp spatiotemporal gradients. To address this, Agarwal et al. [19] proposed a reduced-order model using proper orthogonal decomposition, enabling efficient simulation while retaining physical fidelity. In parallel, artificial neural networks (ANNs), have gained traction as a surrogate models, offering accurate predictions at reduced computational cost. Several studies have demonstrated successful ANN-based optimization strategies trained on data from high-fidelity simulators such as Aspen Adsorption, allowing for rapid evaluation of operational parameters and performance trends [20,21]. [21]A PSA cycle model for a gas mixture ($H_2/CO_2/CO$ = 0.68/0.27/0.05) was developed using a Cu-BTC adsorbent bed and optimized with the Aspen Adsorption platform [22]. This analysis explored the effects of

adsorption pressure, product flow rate, and adsorption time on system performance. Results indicated that increasing adsorption pressures enhances hydrogen purity but reduces recovery, while extended adsorption times and lower product flow rates improve recovery at the expense of purity. To accelerate performance prediction and optimization, an artificial neural network (ANN) model was trained on simulation data generated from Aspen. The ANN demonstrated high accuracy and it was successfully used to identify optimal operating conditions for the PSA cycle. These findings confirm the viability of ANN-based optimization, trained on high-fidelity simulations, for improving PSA performance. Building on this approach, a surrogate-based optimization methodology was introduced for cyclic adsorption processes, with a focus on PSA systems for CO_2 capture [23]. A multiple-input-single-output framework was constructed using two deep neural networks to predict key performance indicators. These models were integrated within a particle swarm optimization algorithm, combined with statistical analysis to construct a detailed Pareto front. This enabled the identification of feasible operating regions and supported informed, multi-objective decision-making. The methodology was validated by comparing optimized results to those from a detailed phenomenological model, demonstrating strong predictive accuracy and robustness.

Despite these developments, PSA optimization remains challenging due to several interdependent issues: (i) gradient-based methods often suffer from high computational demands, particularly when applied to multi-cycle PSA simulations involving sensitive parameters; (ii) failure in sensitivity integration can degrade optimization quality; (iii) repeated simulation calls embedded in optimization frameworks raise overall computational costs; and (iv) full-order stochastic solvers, while capable of broad design-space exploration, offer limited assurance of global convergence [24]. To overcome these challenges, a novel strategy is proposed for multi-objective optimization of PSA systems, based on a Hybrid Surrogate Model (HSM) that combines mechanistic insights with data-driven modeling. The HSM is integrated with the Non-dominated Sorting Genetic Algorithm II (NSGA-II), enabling scalable and computationally efficient optimization across hydrogen purity, recovery, productivity, and energy or cost-related metrics. This hybrid framework establishes a new benchmark in PSA process optimization. The approach is applied to the specific and underexplored problem of industrial-scale PSA cycle optimization for H_2/N_2 separation following ammonia decomposition. Notably, no prior work has reported the optimization of a truly industrial-scale PSA process for this separation. To fill this gap, the present work introduces a novel HSM framework, illustrated in Fig. 1. Multiscale simulations are used to evaluate two adsorbents and generate training data for the surrogate model, which is iteratively refined for improved accuracy. The resulting model supports efficient, multi-objective optimization using NSGA-II, offering practical insights for the design and operation of ammonia-based hydrogen purification systems at scale.

2. System description and methodology

The methodology adopted in this study begins with the development of the PSA process model to generate the dataset. A base-case simulation was first carried out using the operational parameters of the reference design to identify the key variables influencing hydrogen purification unit (HPU) performance. Constraints were then introduced to guide the optimization process. The resulting datasets were used to train the surrogate models. A multi-objective optimization problem was subsequently formulated and solved using both the surrogate and full-order models to determine the Pareto front [24].

2.1. Pressure swing adsorption process to capture N_2

This study targets the PSA-based separation of N_2/H_2 mixtures derived from the decomposition of green ammonia. Under typical conditions achieved by advanced catalytic crackers [25], full ammonia conversion can be assumed, yielding a gas mixture containing 75 % H_2 and 25 % N_2. Trace ammonia can be removed using downstream units such as membranes or commercial adsorbents; this aspect lies beyond the scope of the present study [26] [27]. The HPU employs four parallel adiabatic beds packed with zeolite 5 A, operating in an eight-steps PSA cycle. Figs. 2 and 3 show a schematic and flow sequence of the four-bed

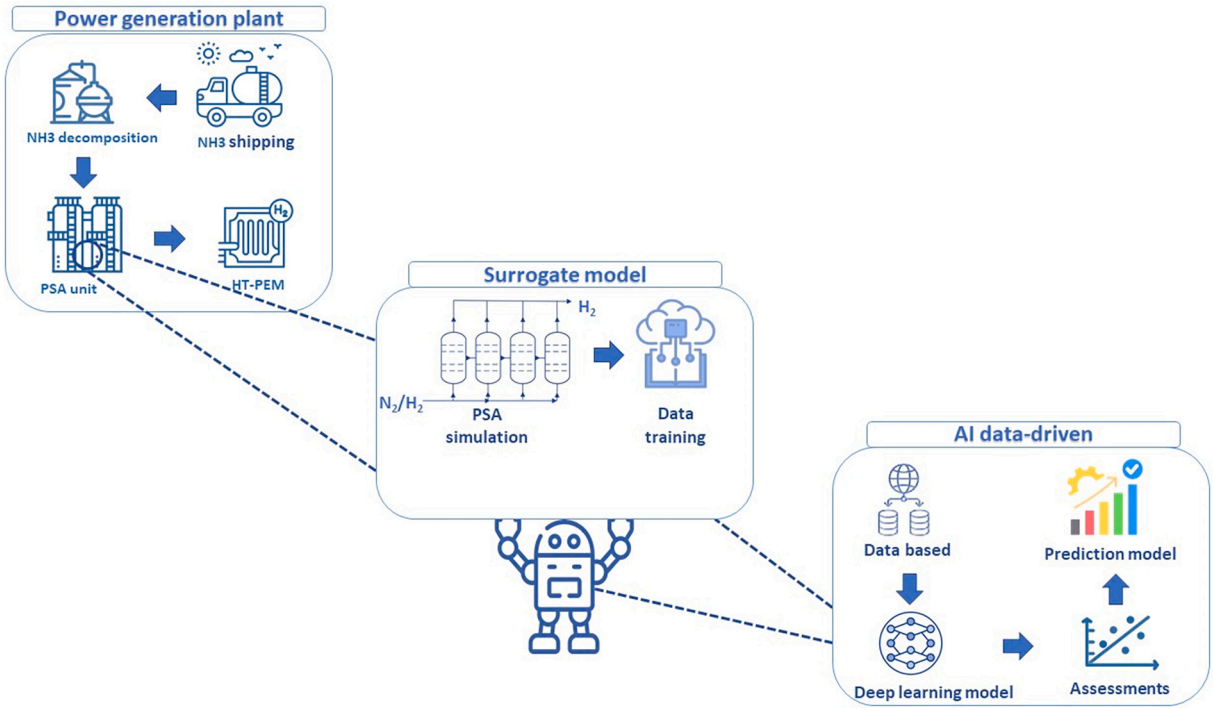

Fig. 1. Schematic representation of the hybrid surrogate modeling framework developed for the design and optimization of the PSA-based hydrogen purification process.

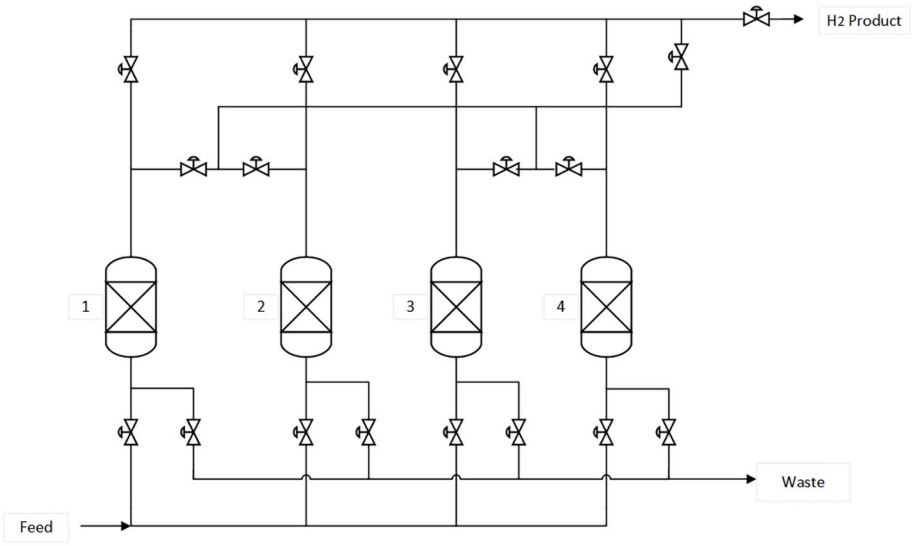

Fig. 2. Schematic diagram of the four-bed pressure swing adsorption (PSA) process used for hydrogen purification, showing the sequence of cycle steps and column configuration.

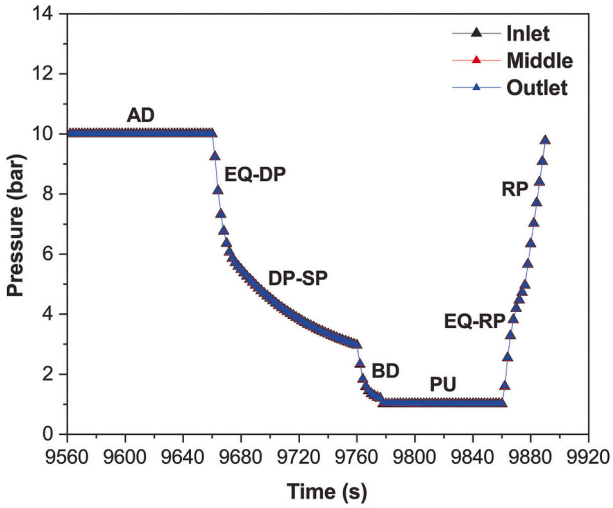

Fig. 3. Flow diagram and cycle sequencing of the four-bed PSA process for hydrogen purification in this study.

process. Each column alternates through the cycle phases: adsorption (A1), equalization (E1), depressurization, purge, re-pressurization, and gas distribution adsorption (AD), equalization (EQ), depressurization (DP), supply to purge (SP), blowdown (BD), purge (PU), re-pressurization (RP).

Table 1
Step durations for the wight-step PSA cycle in the original HPU design.

Time(sec)	Step #	Bed 1	Bed 2	Bed 3	Bed 4
15	1	AD	EQ - RP	BD	EQ - DP
85	2	AD	RP	PU	DP - SP
15	3	EQ - DP	AD	EQ - RP	BD
85	4	DP - SP	AD	RP	PU
15	5	BD	EQ - DP	AD	EQ - RP
85	6	PU	DP - SP	AD	RP
15	7	EQ - RP	BD	EQ -DP	AD
85	8	RP	PU	DP - SP	AD

Table 1 is scheduling for designing of Four-bed PSA cycle simulated in this study. AD: Adsorption, EQ - DP: equalization- depressurization, DP-SP: depressurization - supply to purge, BD: blowdown, PU: Purge, EQ-RP: equalization-repressurization, RP: repressurization.

- In Step 1 (15 s, AD), Bed 1 performs adsorption, while Beds 2 and 4 undergo pressure equalization (EQ-DP), and Bed 3 is in the blow-down (BD) phase.
- In Step 2 (85 s, AD), Bed 1 continues adsorption. Simultaneously, Bed 2 undergoes repressurization (RP) using feed gas, and Bed 4 performs purging (PU) using the gas released from the depressurization of Bed 3.
- In Step 3 (15 s), Bed 1 equalizes pressure with Bed 3 (EQ-DP), Bed 2 enters the adsorption phase, and Bed 4 enters the blowdown step.
- In Step 4 (85 s), Bed 2 continues adsorption. Bed 1 conducts depressurization and supplies purge gas (DP-SP) to Bed 4, and Bed 3 is repressurized with feed gas.
- In Step 5 (15 s), Bed 3 starts adsorption, Beds 2 and 4 perform pressure equalization (EQ-DP and EQ-RP), and Bed 1 enters the blowdown step.
- In Step 6 (85 s), Bed 3 continues adsorption, Bed 2 purges Bed 1 (PU) using gas from Bed 1's previous depressurization, and Bed 4 is repressurized using feed gas.
- In Step 7 (15 s), Bed 4 begins the adsorption step. At the same time, Bed 3 equalizes pressure with Bed 1, and Bed 2 is in the blowdown phase.
- Finally, in Step 8 (85 s), Bed 4 continues adsorption, Bed 3 performs purging using the gas released from the depressurization of Bed 2, and Bed 1 is repressurized with feed gas in preparation for the next cycle.

Fig. 3 illustrates each step of the proposed PSA cycle and the corresponding duration and sequence for all four beds over the eight-step cycle in this study, after reaching steady state. in Step 1 (AD - Adsorption), adsorption occurs for 15 s, during which the pressure is held constant at 10 bar. In this period, beds 2 and 4 undergo pressure equalization, while bed 3 performs a blowdown step. During the EQ-DP (Equalization–Depressurization) step, bed 1 equalizes pressure with bed 3, resulting in a pressure drop in bed 1 to approximately 5.7 bar. In the DP-SP (Depressurization - Supply to Purge) step, the pressure in bed 1 continues to drop, reaching 2.85 bar, In while the released gas is used to purge bed 4. In the subsequent BD (Blowdown) step, bed 1 is further

depressurized to atmospheric pressure. Next, during the PU (Purge) step, bed 2 exhaust gas is used to purge bed 1, maintaining it at atmospheric pressure. Following this, in the EQ-RP (Equalization–Repressurization) step, the pressure in bed 1 is increased to approximately 4.95 bar through pressure equalization. Finally, during the RP (Repressurization) step, feed gas is introduced to raise the pressure back to the adsorption level (10 bar), preparing bed 1 for the next cycle.

2.2. Adsorbents

Two commercially available zeolite molecular sieves, Zeolite 5 A and Zeolite 13X, were evaluated as potential adsorbents for hydrogen purification from H_2/N_2 mixtures. The selection criterion was based on comparative analysis of their adsorption isotherm data, including equilibrium adsorption capacity, selectivity, and working capacity for the components of interest. To quantify the equilibrium uptake, the six-parameter Extended Langmuir-Freundlich isotherm model was fitted to single-component isotherm data for both adsorbents. The comparative analysis, detailed in Section 3.1, revealed that Zeolite 5 A exhibits superior performance characteristics for this separation. Consequently, Zeolite 5 A was selected as the adsorbent material for all subsequent PSA simulations and optimization studies [28,29].

2.3. Modeling

The PSA process was modeled under the following assumptions [30] [31]: (i) The gas phase follows the Peng-Robinson equation of state; (ii) the system is **non-isothermal**, accounting for gas and solid-phase heat conduction, with no external heat exchange (adiabatic wall assumption). The system is effectively adiabatic under the studied conditions, with feed and ambient temperatures equal and negligible external heat exchange. These simplifications are justified within the studied operating range but may limit accuracy under strong radial gradients or significant external heating; (iii) radial gradients in mass, heat, and momentum are neglected due to plug-flow behavior and high Peclet numbers; (iv) mass transfer is described using the linear driving force (LDF) model; (v) pressure drop in calculated via the Ergun equation; (vi) bed porosity is assumed constant. (vii) Local thermal equilibrium is assumed due to rapid heat exchange between the gas and the solid. The governing equations were discretized using an upwind differencing scheme with 20 spatial nodes. Nonlinear solvers were used with a convergence tolerance of 1×10^{-5}. The mathematical formulation included partial and total material balances, energy and momentum conservation, pressure drop, axial dispersion, and equilibrium relationships via the Extended Langmuir-Freundlich isotherm. Key definitions and parameters used include: pressure drop (P), fluid viscosity (μ), density (ρ), particle radius (r_p), bed void fraction (ε_b), molecular weight (M_w), shape factor (ψ), axial dispersion (u_{zk}), and molecular diffusivity (D_{mk}),. Equations are summarized in Table 2.

The physical, structural, and thermodynamic properties of Zeolite 5 A used in the simulation model are comprehensively reported in Table 3.

2.4. PSA scale-up

Scaling up PSA processes from pilot to industrial scale introduces complexities, primarily due to differences in hydrodynamics and heat transfer that influence mass diffusion and overall performance. Pilot-scale systems are commonly used for adsorbent screening and design validation, but their performance does not always translate directly to industrial scale. [34] One of the most widely adopted methods for PSA scale-up is based on the similarity principle, which posits that a process can be transferred from one scale to another by preserving the fundamental physical relationships and dimensionless groups that govern its behavior. The key idea is that if these non-dimensional parameters remain constant, the essential physics of the process are maintained across scales. To implement this approach, the governing mass and momentum balance equations are non-dimensionalized. Each resulting dimensionless group becomes a criterion for scale-up, indicating which parameters must remain unchanged and which may be varied without compromising process performance. By non-dimensionalizing the mass balance equation in PSA systems, it becomes possible to express. [35]

$$\varepsilon_b \frac{L}{u_i}\frac{\partial C_i}{\partial t} = \frac{\varepsilon_b E_{zi}}{u_i L}\frac{\partial^2 C_i}{\partial \bar{z}^2} - \frac{\partial (C_i)}{\partial \bar{z}} - \frac{L}{u_i}\rho_p(1-\varepsilon_b)\frac{\partial Q_i}{\partial t}\ \bar{z} = \frac{z}{L} \quad (8)$$

Where $\bar{z}$ is dimensionless length, $\frac{L}{u_i}$ is the residence time(τ), and $\frac{E_{zi}}{u_i L}$ is the inverse of the Péclet number ($\frac{1}{Pe}$). According to the similarity principle, these parameters are critical and must be preserved during the scale-up of the process. Conversely, some variables, when altered under specific conditions, do not affect the performance of the process [36]. A number of these design variables and the impact of their variations are presented in the Table 4. [36–38]

According to the Table 4, the particle diameter d_p and residence time (τ), are identified as critical design parameters to be kept constant during PSA scale-up, in line with similarity principles. The high Péclet number further confirms the plug flow regime (Table S1, Supplementary Material), ensuring consistent hydrodynamics across scales [37].The resulting scale-up strategy ensures that key dynamic, geometric, and thermodynamic features are conserved, thereby enabling reliable

Table 2
Governing equations used in the PSA model formulation. [32].

Description	Formula (Eq. 1–7)
Partial Material Balance	$\varepsilon_b \frac{\partial C_i}{\partial t} = \varepsilon_b E_{zi}\frac{\partial^2 C_i}{\partial z^2} - \frac{\partial (u_i C_i)}{\partial z} - \rho_p(1-\varepsilon_b)\frac{\partial Q_i}{\partial t}$
Total Material Balance	$C_T \frac{\partial u_g}{\partial z} = -\rho_s \sum_{i=1}^{N_{cmp}} \frac{\partial Q_i}{\partial t}$
Energy Balance	$\frac{\partial^2 T}{\partial z^2}(K_{ga}) - u_g \rho_g C_{vg}\frac{\partial T}{\partial z} - \rho_s \sum_{i=1}^{n_c} \Delta H_i \frac{\partial Q_i}{\partial t} - P\frac{\partial u_g}{\partial z} = \varepsilon_b \rho_g C_{vg}\frac{\partial T}{\partial t}$
Pressure Drop	$\frac{\partial P}{\partial z} = -\left(\frac{1.5\times 10^{-3}(1-\varepsilon_b)^2}{(2r_p\psi)^2\varepsilon_b^3}\mu_g u_g + 1.75\times 10^{-5} M_w \rho_g \frac{(1-\varepsilon_b)}{2r_p\psi\varepsilon_b^3}u_g^2\right)$
Axial Dispersion:	$Ezk = 0.73Dmk + \frac{u_g rp}{\varepsilon_b\left(1+9.49\frac{\varepsilon_b Dmk}{2u_g rp}\right)}$
Extended Langmuir-Freundlich	$Q_i^* = \frac{IP_{1i}\times IP_{2i}P_i^{IP_{3,i}}\exp\left(\frac{IP_{4,i}}{T_s}\right)}{1+\sum_{j=1}^{n_c} IP_{5,j}P_j^{IP_{3,j}}\exp\left(\frac{IP_{6,j}}{T_s}\right)}$
Linear Driving Force	$\frac{\partial Q_i}{\partial t} = MTC_i(Q_i^* - Q)$

Table 3
Properties of Zeolite 5 A used in this study. Data adapted from [33].

Adsorbent's properties	unit	Zeolite 5 A
Adsorbent density (ρ_p)	g/m^3	2.36
Intra-particle porosity (ε_p)	–	0.29
Bulk solid density of adsorbent (ρ_b)	kg/m^3	728
Adsorbent specific heat capacity (c_{ps})	MJ/kg·K	9.21×10^{-4}
Adsorbent thermal conductivity (K_s)	W/m·K	0.46
Adsorbent particle diameter (d_p)	mm	2.06

Table 4
Critical design parameters of the adsorber column used for PSA system modeling. Adapted from [37].

Parameters	Comments
L/U_i	Critical
d_p	Critical
L/d_p	Minimal effect if higher than 150
L/D	Minimal effect if higher than 5
D/d_p	Minimal effect if higher than 30
Re	Minimal effect if higher than 10

extrapolation of performance from pilot to full-scale systems. Bed specifications for the three simulated scales, pilot 1, pilot 2, and industrial, are provided in Table S1 of the Supplementary Material [33].

2.5. Fundamental design variables of the PSA processes

The performance of a PSA system depends on a wide range of design and operational variables. Among the most critical are the geometric dimensions of the bed (length and diameter), adsorption pressure, operating temperature, and feed flow rate. Selecting these variables appropriately is essential to ensure that the process operates within optimal performance bounds. Performance evaluation is typically based on four main indicators: hydrogen purity and recovery, productivity, and the specific energy consumption (SEC), Table 5. Hydrogen purity and recovery are generally treated as the primary objective functions to be maximized, while SEC is minimized. In Table 6 the performance indicators equations are given. Where: C_{H2} is the hydrogen concentration (mol/m^3), u the superficial velocity (m/s), t_{des}, t_{ads}, t_{cycle} are the desorption, adsorption, and total cycle time (s), respectively . $\gamma = \frac{c_p}{c_v}$, η the mechanical efficiency (typically assumed as 0.8), R the universal gas constant (J/mol·K), T the temperature (°C), $\dot{B}$ the molar flow rate to be compressed (kmol/h), P_{out} and P_{in} are the outlet and inlet pressures (bar) in the compression system, respectively.

2.6. Surrogate model development

2.6.1. Data generation and pre-processing

To construct an accurate and generalizable surrogate model, it is essential to train it on a broad, diverse, and high-quality dataset. In this work, simulation input data were generated using the Latin Hypercube Sampling (LHS) method, which ensures uniform coverage of the design space while minimizing the number of required samples [41]. A dedicated Visual Basic for Applications (VBA) interface was developed to automate data extraction from the Aspen Adsorption® simulation environment and export it to Microsoft Excel for further processing. Five key variables were selected as inputs to represent the PSA operating conditions: adsorption pressure (P_{ads}), bed length (L), bed diameter (D), adsorption temperature (T_{feed}), and flow rate (F_{feed}). A total of 2000 simulation runs were performed using LHS across the full range of these decision variables. For each simulation, H_2 purity, H_2 recovery, productivity, and SEC were calculated.

To ensure balanced training and avoid bias, all input variables were normalized prior to training the models, as they span different orders of magnitude.

2.6.2. Surrogate model configuration

Four commonly used machine learning algorithms were employed to build the surrogate models within the hybrid optimization framework integrated with the Non-dominated Sorting Genetic Algorithm II (NSGA-II). Among these, the Multi-Layer Perceptron (MLP) was selected as the primary architecture. An MLP is a type of feedforward artificial neural network comprising an input layer, one or more hidden layers, and an output layer. The input layer corresponds to the dimensionality of the selected decision variables. The hidden layers introduce nonlinearity and enable the model to capture complex interactions among process variables. The output layer maps the network outputs to the desired performance indicators. Weights connecting neurons across layers were initialized randomly (typically in the range 0–1) and refined through backpropagation during training [42]. The training and implementation of the ANN were performed using MATLAB. The MLP surrogate model consists of two hidden layers with 12 and 6 neurons, respectively, optimized via a Genetic Algorithm. *tansig* activation was used in the hidden layers and *purelin* in the output. The dataset was split 70 % for training and 30 % for validation/testing. Early stopping (*max_fail* = 6), a minimum gradient of 1×10^{-9}, and a maximum of 1000 training epochs were employed to ensure convergence and prevent overfitting. Once the surrogate model was trained and validated, it was used to support multi-objective optimization of the PSA process using the Non-dominated Sorting Genetic Algorithm II (NSGA-II). The optimization aimed to simultaneously maximize hydrogen recovery and purity, and minimize SEC. These objectives were formulated into a nonlinear programming (NLP) problem, where the surrogate model acts as a rapid-response function evaluator. Table 6 provides the full definition of the objective functions and constraints applied to the decision variables (feed rate, temperature, pressure, bed dimensions).

Table 5
Definitions and formulas of key performance indicators used to evaluate PSA system performance [39,40].

Performance Indicators	Unit	Formula (Eq. 9–12)
N_2 average impurity	–	$\frac{\int_0^{t_{ads}} C_{N_2} u\|_{z=L} dt}{\sum_{i=1}^{m} \int_0^{t_{ads}} C_i u\|_{z=L} dt}$
Hydrogen recovery	–	$\frac{\int_0^{tads} (C_{H_2} u\|_{z=L}) dt}{\int_0^{tads} (C_{H_2} u\|_{z=0}) dt}$
Hydrogen productivity	kmol/kg·h	$\frac{\int_0^{tads} C_{H_2} u\|_{z=L} dt}{w_{adsorbent} t_{cycle}}$
SEC	MJ/kg_{H2}	$\frac{\int_0^{tcycle} \frac{\gamma}{\gamma-1} \frac{RT}{\eta} \dot{B} \left[\left(\frac{P_{out}}{P_{in}} \right)^{\frac{\gamma-1}{\gamma}} - 1 \right] dt}{\int_0^{tads} (C_{H_2} u\|_{z=L}) dt}$

Table 6
Formulation of the multi-objective optimization problem for the PSA process, including decision variables, objective functions, and operational constraints.

Minimize $f_i(x)$	$X = F_{feed}, T_{feed}, P_{ads}, L, D$
Where:	$f_1 = -$ Hydrogen recovery (−) $f_2 = -$ Hydrogen purity (−) $f_3 =$ SEC (MJ/kg_{H2})
Subject to:	$60 < F_{feed} < 150$ kmol/h $10 < T_{feed} < 50$ °c $6 < P_{ads} < 12$ bar $0.7 < D < 1.2$ m $1.7 < L < 4.5$ m

2.6.3. NSGA-II for multi-objective optimization

In multi-objective optimization problems, conflicting objectives lead to a set of optimal solutions (Pareto front) rather than a single optimal solution. No one solution on this front can be universally considered superior without specific decision-making preferences. Traditional optimization methods often reduce such problems to single-objective formulations, which require solving the problem repeatedly to identify multiple trade-off solutions, an inefficient and computationally expensive approach. By contrast, multi-objective evolutionary algorithms (MOEAs), and specifically the NSGA-II, are capable of identifying multiple Pareto-optimal solutions in a single run. By operating on a population of solutions, EAs can be adapted to maintain solution diversity while converging toward the true Pareto-optimal front. This inherent parallelism allows for efficient exploration of the solution space without the need for multiple iterations [40].

The NSG-II algorithm was implemented in MATLAB and coupled with the PSA simulator to optimize the proposed cycle. The integration of NSGA-II with the PSA surrogate model is shown in Fig. 4. The workflow proceeds as follows: (i) An initial population is generated, with each individual representing a specific combination of decision variable values; (ii) Each solution is passed to the surrogate-based PSA simulator, which rapidly evaluates the key performance indicators: H_2 purity, H_2 recovery, productivity, and SEC; (iii) The evaluated solutions are sorted into non-dominated fronts, and each front is internally ranked by crowding distance; (iv) A selection mechanism (binary tournament selection) chooses individuals for reproduction based on both front rank

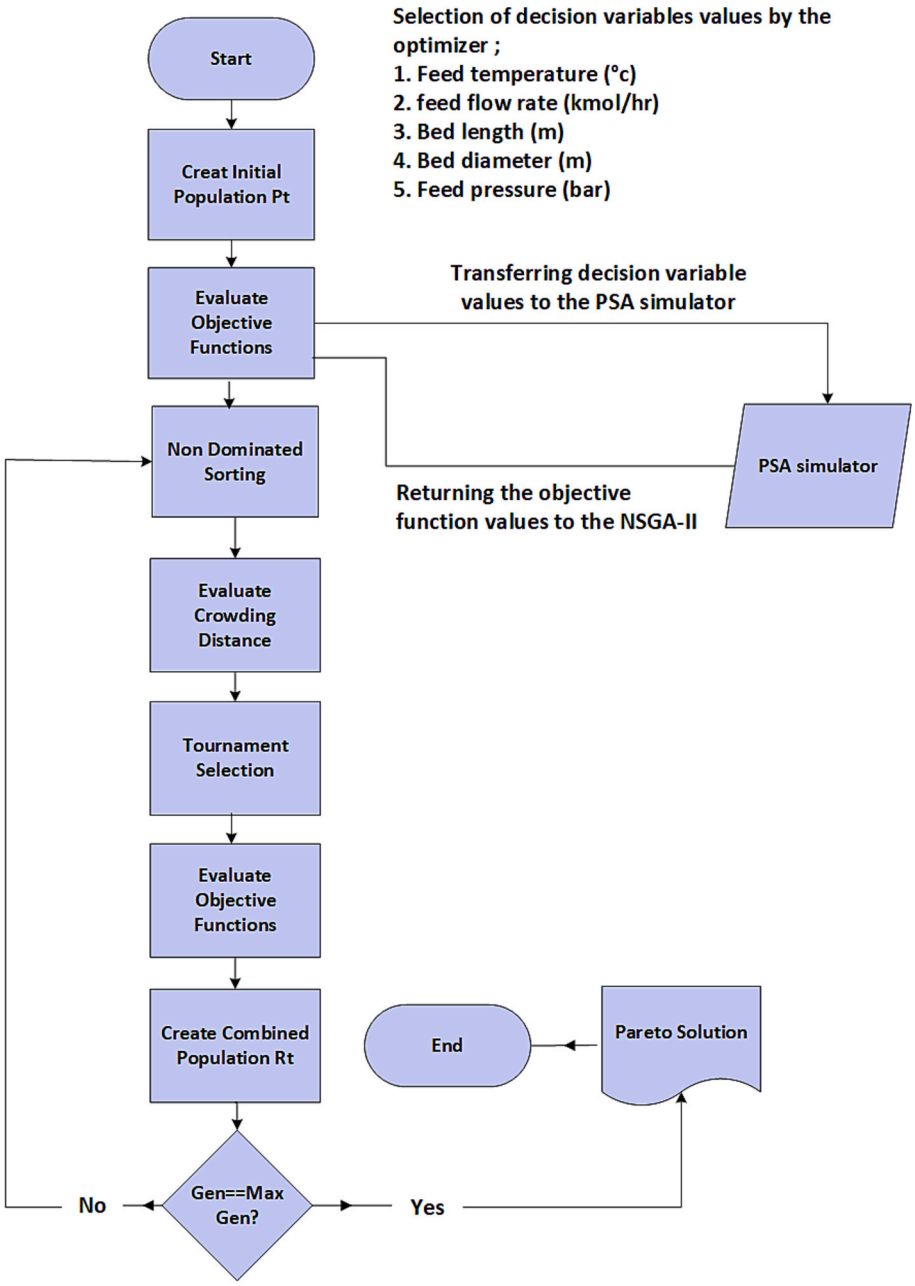

Fig. 4. Overview of the optimization framework developed in this study, integrating surrogate modeling and multi-objective optimization for PSA process design.

and crowding; (v) Crossover and mutation operators generate new offspring; (vi) The new population is evaluated, merged with the previous one, and sorted again; (vii) The process repeats until the maximum number of generations is reached or convergence criteria are met. To ensure an appropriate balance between computational cost and solution accuracy, parameter values were selected through trial-and-error. In this work population size was set to 400, with a maximum of 2500 generations, a crossover and mutation probability of 0.9 and 0.1, respectively, and a crossover and mutation index of 20. The optimization was terminated early if no significant improvement was observed in the objective functions over consecutive generations. The bounds for the five decision variables used in the optimization are summarized in Table 6.

2.6.4. *Economic assessment for building purified hydrogen*

The economic viability of the PSA unit was assessed using Aspen Process Economic Analyzer, considering capital expenditure (CAPEX), operating expenditure (OPEX), product sales revenue, and pay-out period for the three optimal designs identified via multi-objective optimization. Total capital cost includes direct costs (adsorption columns, Zeolite 5 A adsorbent, piping and valves, instrumentation and control systems, compressor, and installation) and indirect costs (engineering, construction overhead, contractor fees, and contingency). Equipment costs were estimated using Aspen Economics correlations based on capacity, materials, and operating conditions, with all costs indexed to the current year using the Chemical Engineering Plant Cost Index (CEPCI). Annual operating cost encompass utilities, raw materials, labor, maintenance, and overhead. Product revenue was calculated from hydrogen production rates and current market prices for high-purity hydrogen. The pay-out period (POP = Total Capital Cost / (Annual Revenue - Annual Operating Cost)) represents the time required to recover the initial investment from net annual profits.

3. Results and discussion

3.1. Process simulation

To quantify the equilibrium uptake, the six-parameter Extended Langmuir–Freundlich isotherm model was fitted to experimental single-component isotherm data [43,44] for two adsorbents (zeolite 5 A and 13X) The fitting results for N_2 and H_2, at different temperatures as function of the operating pressure, are shown in Fig. 5.

In Fig. 5(a), hydrogen shows higher uptake on the 13X adsorbent compared to 5 A. Although the 5 A adsorbent, operating at a lower temperature (288 K), would be expected to exhibit higher H_2 adsorption capacity compared to 13X at (298 K), 13X still demonstrates superior hydrogen adsorption performance. In Fig. 5(b), nitrogen exhibits a higher adsorption affinity on 5 A up to 8 bar; however, above this pressure, N_2 shows slightly greater uptake on the 13X adsorbent. The parameters estimated from the fitting are reported in Table 7. Based on these considerations, zeolite 5 A was selected as the adsorbent for subsequent PSA cycle modeling and optimization.

To further validate the dynamic behavior of the adsorption bed and the reliability of the model, breakthrough experiments were analyzed. Fig. 6 compares simulation results with both experimental data and a previous numerical study for multicomponent adsorption at a flow rate of 1.3×10^{-3} kmol/h, under conditions of 1 bar and 40 °C [33,45]. Despite the inherent simplifications adopted in the model, the dynamic simulations show good agreement with both experimental and simulated breakthrough curves, particularly in terms of temperature and concentration profiles.

Fig. S1. (Supplementary Material) shows the simulated breakthrough curves for the binary H_2-N_2 system. N_2 breaks through at approximately 200 s, with the outlet concentration reaching 0.25 %, while H_2 concentration decreases correspondingly to 75 %. The model was validated against experimental multi-component data ($H_2/N_2/Ar/CH_4$) from the literature [33], as shown in Fig. 7. Notably, the N_2 breakthrough time in the binary system (~200 s) matches exactly with the reference multi-component case, confirming the model accuracy. This breakthrough time applies to fresh, fully regenerated adsorbent; in cyclic PSA operation, residual N2 loading remains after each cycle, creating adsorption resistance that reduces breakthrough time relative to fresh adsorbent.

3.2. Sensitivity analysis

To ensure optimal PSA performance for hydrogen recovery, it is essential to understand how key operating parameters affect the process performances. One-at-a-Time Local Sensitivity Analysis (OAT-LSA) was conducted to investigate the effect of five decision variables: bed length, bed diameter, flow rate, adsorption pressure, and temperature, on four principal performance indicators: hydrogen purity, hydrogen recovery, hydrogen productivity, and SEC. As shown in Figs. 7 and 8, each operating variable exerts a significant, and frequently nonlinear, influence on system behavior. These trends underscore the conflicting nature of the performance objectives, indicating that single-objective optimization are inadequate. A multi-objective optimization framework is therefore required to simultaneously balance these trade-offs and identify optimal operating regimes. The sensitivity analysis confirms the strong influence of each parameter and further justifies their selection as decision variables in the surrogate-based optimization model. By capturing the complex interdependencies between variables using machine learning, to the surrogate model enables efficient exploration of the design space and reliable generation of a Pareto front using NSGA-II.

Fig. 7a illustrates the impact of adsorption pressure on purity and recovery, and Fig. 7b illustrates the impact of adsorption pressure on productivity and SEC. recovery and productivity have the same behavior. As pressure increases, hydrogen purity improves due to enhanced adsorption of nitrogen, the heavier component. Additionally, as the pressure increases, the decrease in superficial velocity leads to longer gas-solid contact time, which further enhances N_2 uptake. However, this also results in greater hydrogen retention, lowering overall recovery. These findings highlight the trade-off between purity and recovery at elevated pressures, reinforcing the need for careful optimization. Operating pressure exerts a direct influence on SEC, as shown in Fig. 7b. A higher value of this variable results in increased compressor energy requirements. Among all the decision variables, pressure and bed diameter have the most significant impact on SEC.

According to Fig. 7c and d, increasing the feed temperature generally leads to lower hydrogen purity but higher recovery and a direct influence on SEC.

As shown in Fig. 8e and f, increasing the feed flow rate leads to lower hydrogen purity but higher recovery. This is primarily because increased flow accelerates cycle dynamics, allowing less time for full separation, but also reduces hydrogen loss during desorption and repressurization.

According to Fig. 8b and d, productivity exhibits a trend similar to hydrogen recovery. Increasing the bed length and diameter improves separation efficiency by increasing the amount of adsorbent available. However, this enhancement also leads to greater retention losses and elevated energy consumption, thereby increasing the SEC.

In Figs. 8a-d, it is evident that increasing bed length and bed diameter enhances hydrogen purity. However, this improvement comes at the expense of recovery and productivity, which decrease with increasing bed size. This is attributed to greater hydrogen losses during the blowdown step and higher feed requirements during repressurization. While increasing adsorbent mass improves separation

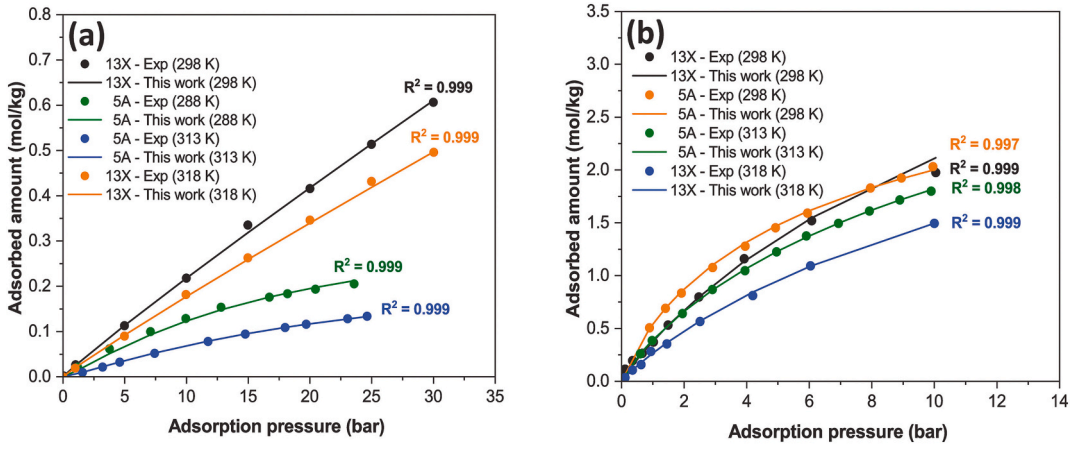

Fig. 5. Adsorption isotherms of H2/N_2 at different temperatures on two adsorbents: (a) H_2 (b) N_2. Solid circles represent experiment data for H_2 and N_2, while solid lines the fits obtained using the Extended Langmuir-Freundlich model [43] [44].

Table 7
Fitting parameters of the Extended Langmuir–Freundlich model for N_2 and H_2 adsorption on 5 A and 13X zeolites.

Adsorbents	Components	Isotherm Parameters					
		IP1	IP2	IP3	IP4	IP5	IP6
Zeolite 5 A	N_2	0.000394	0.000394	0.85454	2481.35	3.59E-07	3911.758
	H_2	1.004E-05	0.00015	1.18212	2580.071	2.41E-04	1429.640
Zeolite 13X	N_2	0.00120	0.00130	0.92141	1653.977	0.05902	55.5511
	H_2	0.00093	0.00100	0.94270	975.973	0.00019	121.833

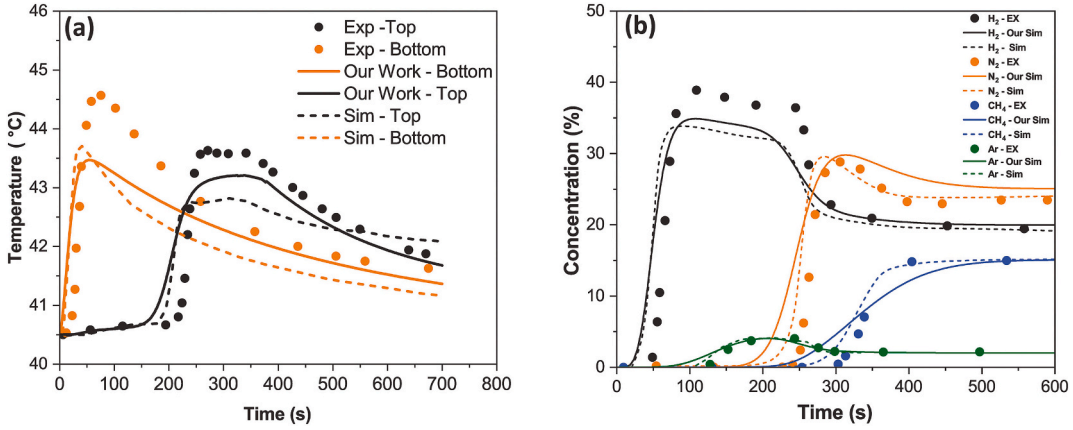

Fig. 6. Comparison of multicomponent breakthrough curves for the temperature and concentration at 1.3×10^{-3} kmol/h, 40 °C, and 1 bar. Solid lines show our simulation results, dotted lines represent previous simulations, and markers indicate experimental data. [33,45].

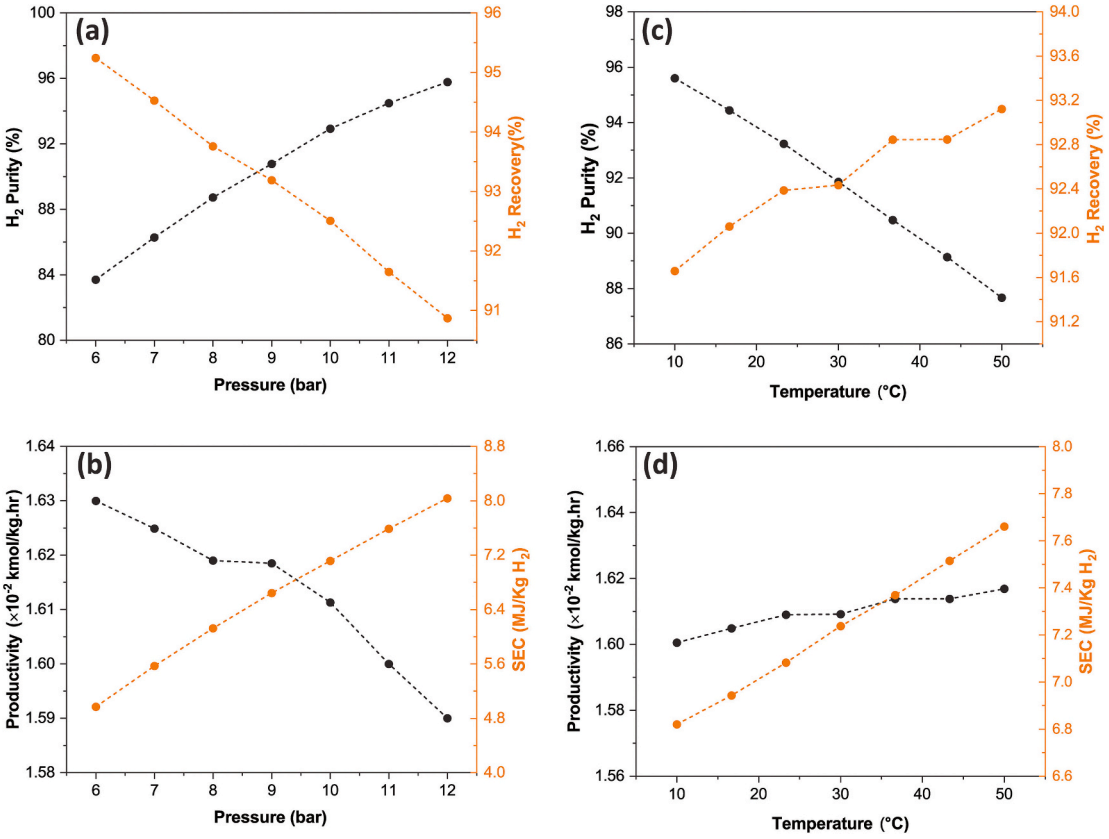

Fig. 7. Effect of decision variable on H_2 purity and recovery.

performance, it also introduces higher retention losses and energy demands. These results emphasize that overdesigning the adsorbent bed can significantly reduce process efficiency. As shown in Figs. 8e and f, increasing the feed flow rate leads to a reduction in SEC. This behavior is attributed to the trade-off between recovery and SEC: as flow rate increases, H_2 recovery improves, resulting in a more favorable SEC

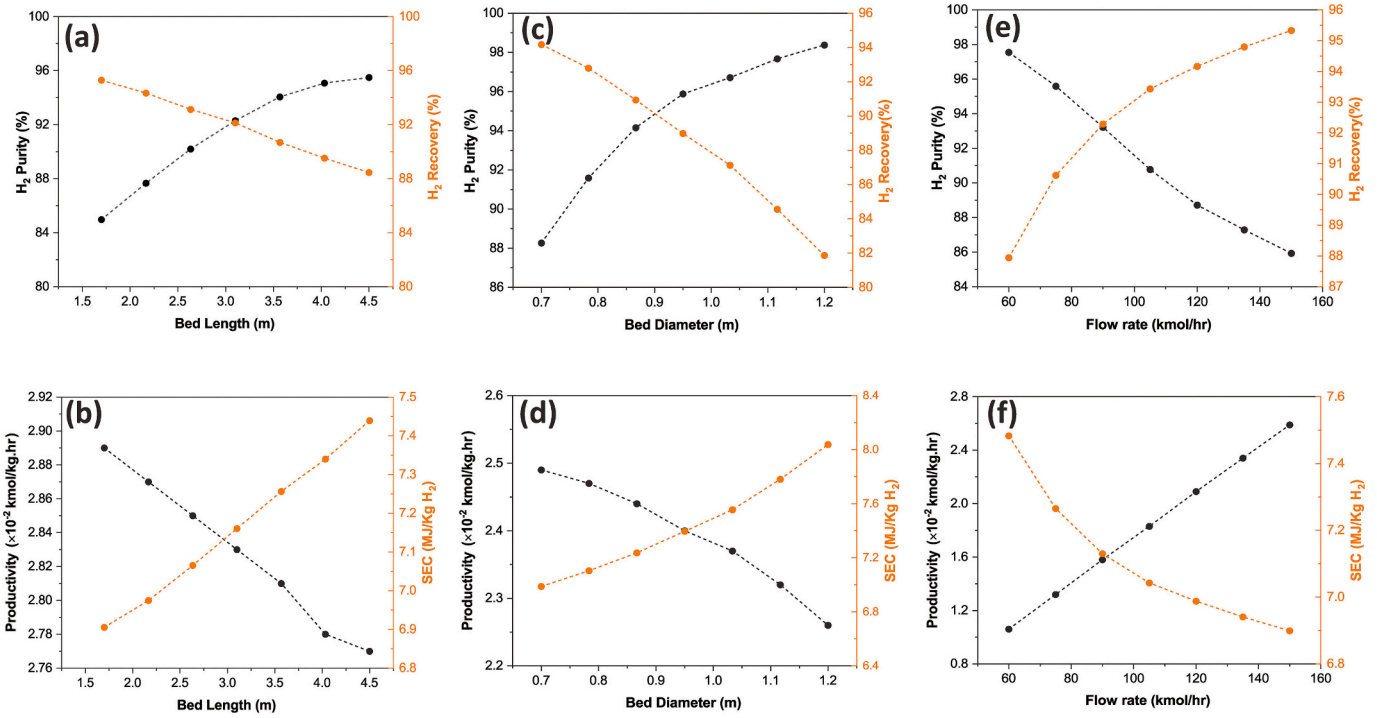

Fig. 8. Effect of decision variable on H_2 productivity and SEC.

performance. Among all the decision variables, pressure and bed diameter have the most significant impact on SEC.

Collectively, these results demonstrate the intricate interactions among operating parameters and justify the application of a multi-objective optimization strategy to achieve an effective balance between separation performance and energy efficiency.

3.3. Surrogate model validation

The validation approach was designed to demonstrate the ability of the ANN surrogate model to both accurately reproduce the training data and generalize to previously unseen operating conditions. To this end, a testing subset of the pseudo-experimental dataset was reserved and not employed during the training phase. Fig. S2 (Supplementary Material) illustrates the predictive performance of the surrogate model on this unseen dataset. The excellent agreement between predicted and actual values confirms that the surrogate model is capable of reliably forecasting outputs beyond its training domain, thereby validating the robustness and generalization capability of the ANN framework.

3.4. Multi-objective optimization results

The three-dimensional Pareto front for H_2 purity, recovery, and SEC is shown in Fig. 9 . This surface illustrates the optimal trade-offs

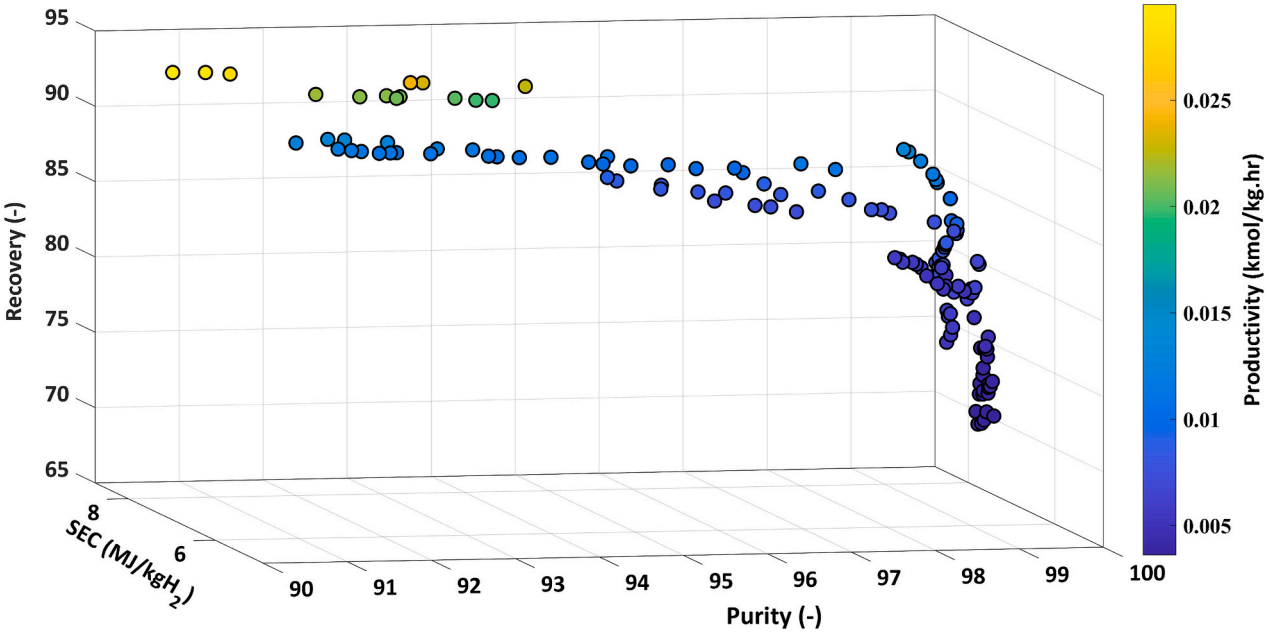

Fig. 9. Three dimensional Pareto fronts showing hydrogen purity, SEC, and recovery.

obtained by simultaneously maximizing purity and recovery while minimizing SEC. As expected, the Pareto solutions reveal that increased recovery generally corresponds to higher productivity.

Fig. 10 presents the relationship between decision variables and the corresponding Pareto-optimal solutions in terms of purity and recovery. In Fig. 10a, the optimizer identifies two distinct regions of bed diameter where ultra-high purity levels (up to 99.99 %) are achievable. These solutions correspond to diameters of approximately 0.96 m and 1.2 m, with varying combinations of feed pressures (6–7 bar or 10–12 bar), flow rates (60–100 kmol/h), and temperatures (10–20 °C and 30–50 °C). As previously noted in the sensitivity analysis, increasing feed pressure enhances separation performance by favoring nitrogen adsorption, thereby improving hydrogen purity. However, this improvement comes at the cost of recovery and compressor energy demand, both of which negatively affect SEC. Similarly, increasing bed length and diameter extends gas-solid contact time, further improving purity, but reducing recovery and increasing SEC due to greater hydrogen retention and feed requirements during repressurization. Lowering flow rate has a comparable effect: it enhances hydrogen purity through improved mass transfer but reduces recovery, which increases the SEC denominator. However, it also reduces compressor load, decreasing the numerator, illustrating a dual effect on SEC. Temperature behaves similarly: lower temperatures increase adsorption capacity and improve hydrogen purity, but reduce recovery. At the same time, they decrease gas volume and compressor work, which partially offsets SEC increases. Therefore, temperature exerts opposing influences on SEC, depending on the balance of these factors. To achieve ultra-high purity, the optimized favors high feed pressure, long beds, large diameters, low flow rates, and low temperatures.

For instance, at a diameter of 0.96 m, the optimizer opts for a higher pressure (10 bar), which results in a SEC of 8.6 MJ/kg H_2. In contrast, at a larger diameter (1.2 m), the optimizer achieves the same purity while reducing SEC to 7.8 MJ/kg H_2. This demonstrates a trade-off: larger diameters enable lower-pressure operations with less energy input, by increasing cross-sectional area and reducing pressure drop. Fig. 10b highlights the strong, direct correlation between bed length and hydrogen purity. For all ultra-high-purity designs, the optimizer selected beds longer than 4 m, which is consistent with PSA theory: longer beds provide extended mass transfer zones, delay breakthrough, and allow deeper impurity removal [46]. Interestingly, this also enables operation at moderate pressures, helping balance purity targets against operational costs and equipment constraints. In Fig. 10c, the optimizer shows flexibility across a range of feed temperatures, indicating its ability to compensate for thermal effects by adjusting other variables (e.g., cycle scheduling or pressure). Nonetheless, the highest purities are typically achieved at lower temperatures (~10 °C), confirming trends from the sensitivity analysis.

Fig. 10d shows that high purity designs emerge across three distinct pressure ranges, including lower pressures (around 6 bar) where the optimizer significantly adjusted other variables to compensate. For high-flow-rate designs, pressure was pushed toward the upper limit (12 bar) to maintain sufficient adsorption driving. This aligns with PSA thermodynamics, where increased pressure promotes higher adsorbent loading and improved purity. In Fig. 10e, the optimizer generally associates higher flow rates with greater hydrogen recovery, as increased flow improves adsorbent utilization per cycle. However, maintaining high purity under these conditions required concurrent adjustments, increasing pressure and bed length, to preserve separation performance. This illustrates the optimizer's ability to coordinate multiple trade-offs across kinetic and equilibrium boundaries.

The influence of design variables on SEC (MJ/kg H_2) is shown in Figs. 11a-e. The relationship between feed flow rate and SEC exhibits a dual behavior: in designs where hydrogen production dominates (i.e., high cycle productivity), increasing flow reduces SEC due to enhanced throughput relative to energy input. Conversely, in energy-dominated designs, increasing flow elevates SEC due to increased compressor load and switching losses. Overall, the optimizer successfully balances these competing effects, locating operating conditions that minimize SEC while still satisfying hydrogen purity and recovery requirements. These insights provide a valuable decision-making framework for selecting PSA operating conditions based on process priorities, whether favoring ultra-high purity, high recovery, or minimal energy consumption.

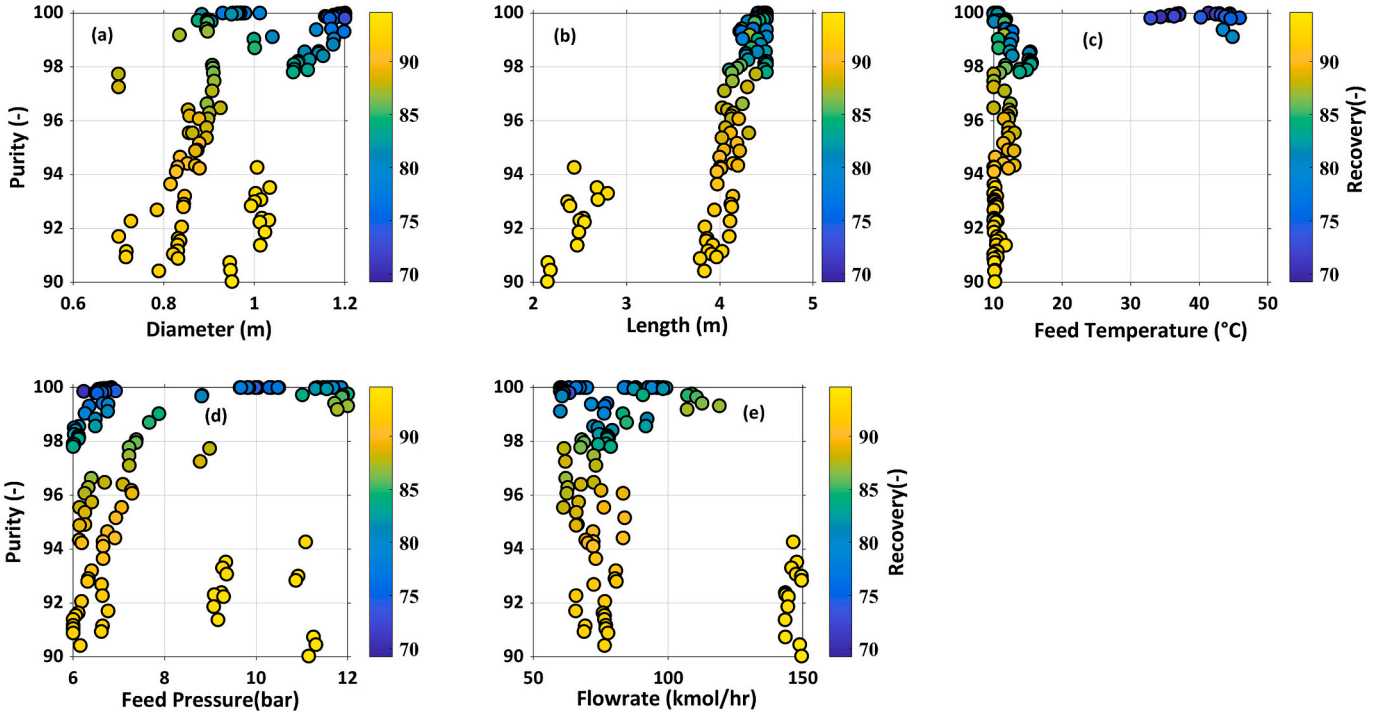

Fig. 10. Decision variables plotted against Pareto solutions for hydrogen purity and recovery.

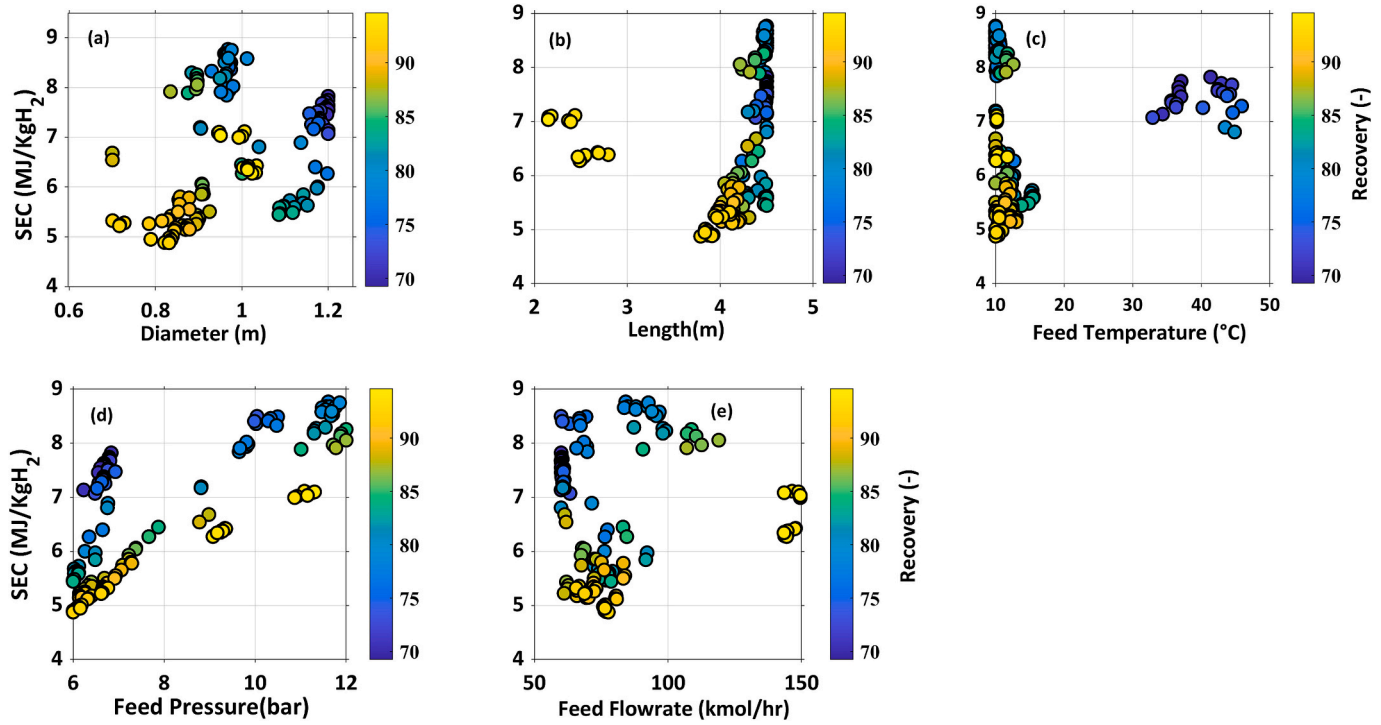

Fig. 11. Decision variables plotted against Pareto solutions for SEC and recovery.

3.5. Optimal design discussion

The Pareto front analysis reveals three distinct operating regions (Fig. 12), each corresponding to a unique process design with different trade-offs between hydrogen purity, recovery, and energy consumption (Table 8). Importantly, none of these regions universally dominates the others in all objectives; rather, each represents a different optimization strategy based on process priorities. Although most applications require hydrogen concentrations above 98 %, results with purity down to 90 % are reported because such mixtures are relevant for specific applications. In the context of this work, unlike low-temperature PEM fuel cells, high-temperature PEM fuel cells and solid oxide fuel cells can tolerate nitrogen concentrations up to 20 %, with only a minor reduction in performance [7]. In these cases, PSA systems optimized for intermediate purities can provide higher recovery and lower cost than designs targeting >98 % purity.

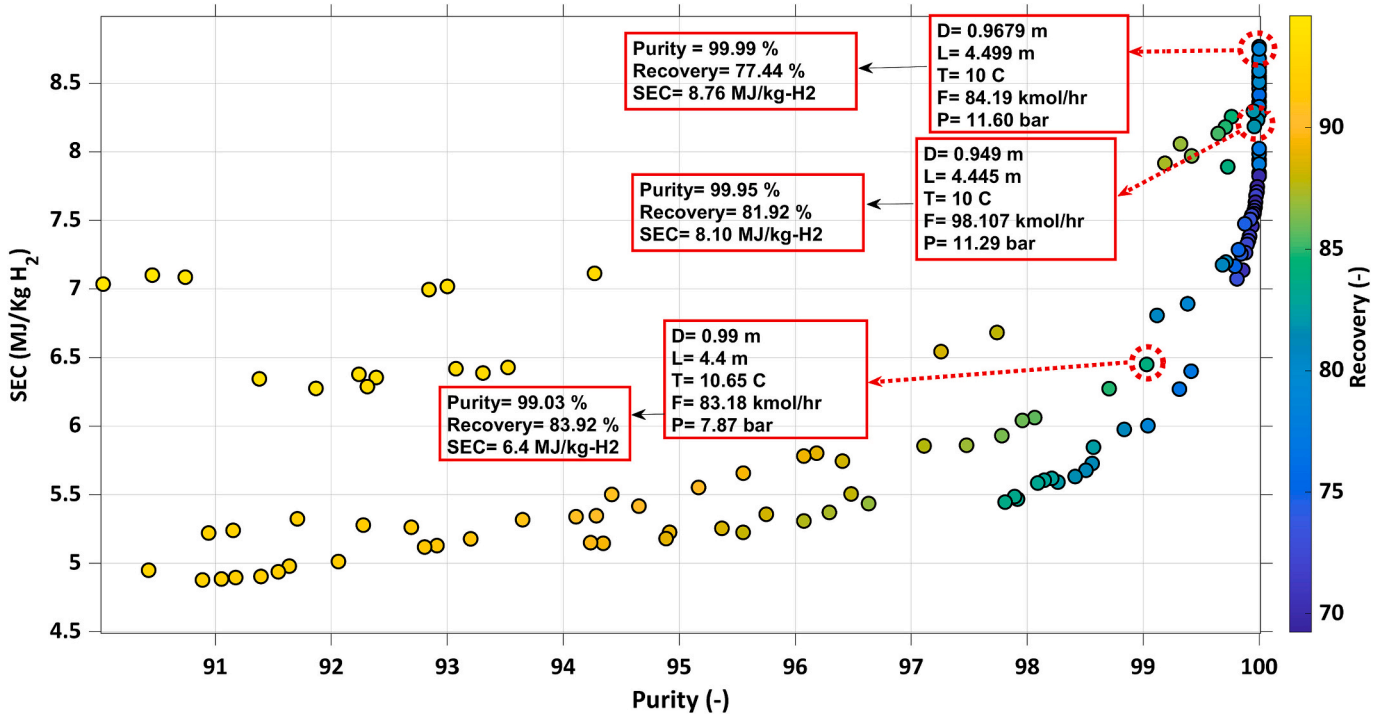

Fig. 12. Two-dimensional Pareto front showing hydrogen purity, SEC, and recovery.

Table 8
Decision variable values and corresponding simulation results for process indicators in two case studies.

Design variables					
	D(m)	L(m)	T(°c)	F(kmol/h)	P_{ads}(bar)
Simulation	0.866	3	25	92	10
Optimal (1)	0.9679	4.499	10	84.19	11.60
Optimal (2)	0.949	4.445	10	98.107	11.29
Optimal (3)	0.99	4.4	10.65	83.18	7.87

Performance indicators			
	Purity of H_2(−)	Recovery of H_2(−)	SEC(MJ/kg_{H2})
Base case simulation	96.35	91.1	7.2
Optimal design (1)	99.99	77.44	8.76
Optimal design (2)	99.95	81.92	8.10
Optimal design (3)	99.03	83.92	6.4

In Region 1, the optimizer achieves ultra-high purity (99.99 %), with a recovery of 77.44 % and a SEC of 8.76 MJ/kg_{H2}. This design is characterized by the maximum bed length (4.5 m) and inlet pressure (11.6 bar), as well as the lowest feed temperature (10 °C). The bed diameter is relatively large (0.9679 m), and the feed flow rate is maintained at 84.19 kmol/h. Although this configuration offers the sharpest separation profile, it incurs the highest SEC, due to increased compressor duty at elevated pressure and reduced recovery. This design is suitable when purity is the overriding objective, regardless of energy cost.

In Region 2, bed length, diameter, and pressure are slightly reduced compared to Region 1, while the feed temperature remains low (10 °C). The flow rate increases to 98.107 kmol/h. These adjustements yield a hydrogen purity of 99.95 %, a recovery of 81.92 %, and a reduced SEC of 8.10 MJ/kg_{H_2}. This region reflects a more balanced trade-off, where slight compromises in purity enable significant gains in both recovery and energy efficiency. Region 3 demonstrated the optimizer's ability to shift toward energy-saving designs. Here, the inlet pressure is substantially lowered, while the bed length and diameter remain near their maximum values. The feed temperature is marginally increased to 10.65 °C, and the flow rate is reduced to 83.18 kmol/h. These conditions result in a purity of 99.03 % recovery rate of 83.9 %, and a significantly improved SEC of 6.4 MJ/kg-H_2. Although there is a modest drop in purity, the energy savings are substantial, making this configuration attractive for cost-sensitive or efficiency-focused applications.

Table 9 presents a preliminary economic assessment of the three proposed zones, highlighting trade-offs among capital expenditure (CAPEX), operational expenses (OPEX), and return on investment. Zone 1, targeting ultra-high hydrogen purity (99.99 %), requires the highest CAPEX (~$8.56 M) and OPEX (~$6.93 M/year) due to substantial compression energy, but generates the largest annual revenue (~$9.5 M) with the shortest payback period (3.33 years), making it suitable where purity is critical. Zone 2 offers a balanced purity-recovery profile, slightly higher CAPEX and OPEX than Zone 1, similar revenue, and a payback of 4.41 years, representing a moderate investment option. Zone 3 prioritizes energy efficiency, with lower CAPEX (~ $8.38 M) and OPEX (~ $6.8 M/year), due to reduced pressure and energy use; it produces lower revenue (~ $7.98 M/year) and a longer payback (7.10 years), making it suitable for cost-sensitive or sustainability-focused applications. These results show that economic performance closely follows process priorities, with each configuration presenting feasible trade-offs for its intended use.

Table 9
Economic indicators for the three optimal PSA designs.

Economic indicators				
	Total Capital Cost ($million)	Operating cost ($million/Year)	Product sales ($million/Year)	Pay-out period (Year)
Optimal design (1)	8.556	6.926	9.494	3.332
Optimal design (2)	8.6104	7.8288	2.7882	4.412
Optimal design (3)	8.3879	6.801	7.983	7.096

3.6. *Pareto solution validation of surrogate model with full order*

To evaluate the predictive performance of the surrogate model, the optimized solutions from the final generation of the NSGA-II algorithm, obtained through the integration of Aspen Adsorption and MATLAB, were used for validation against full-order simulations. As shown in the parity plots in Fig. 13, the surrogate model shows excellent agreement with the high-fidelity Aspen model across all key performance indicators: specific energy consumption (SEC), hydrogen purity, productivity, and recovery. The close alignment between surrogate predictions and detailed simulation results confirms the high accuracy and robustness of the developed model. This validation step confirms the surrogate model suitability for multi-objective optimization workflows, enabling approximately 600-fold acceleration in computational time compared to direct full-order simulations, while maintaining high predictive accuracy in exploring PSA design alternatives.

4. Conclusions

- This study presents a comprehensive framework for the modeling, design, and multi-objective optimization of a pressure swing adsorption (PSA) process for hydrogen purification following ammonia decomposition. The methodology integrates mechanistic process modeling with machine learning techniques to enable fast and accurate optimization across competing objectives.
- A high-fidelity PSA model was developed and validated using experimental data. To overcome the computational burden of repeated simulations, a surrogate model was trained and successfully integrated with the NSGA-II optimization algorithm, achieving a speedup of several orders of magnitude in evaluating design alternatives. The resulting Pareto front highlights the inherent trade-offs between hydrogen purity, recovery, and specific energy consumption (SEC). While recovery trends closely with productivity, increasing hydrogen purity leads to a sharper decline in both recovery and SEC.
- Analysis of the Pareto-optimal solutions reveals that:
- Ultra-high purity designs (up to 99.99 %) are associated with high feed pressure (11.6 bar), long beds (4.49 m), larger diameters (0.96 m), lower flow rates (84.2 kmol/h), and low feed temperatures (10 °C).
- High-grade purity designs (around 99.9 %) can be achieved with slightly lower pressures (11.2 bar), shorter beds (4.44 m), similar diameters (0.94 m), higher flow rates (98.1 kmol/h), and the same feed temperature.
- The optimal design configurations demonstrate significant performance gains compared to the base-case scenario, with improvements of up to 2.78 % in hydrogen purity and 11.11 % in SEC.
- Overall, the proposed framework provides a robust and scalable approach for the design and optimization of PSA systems for industrial hydrogen purification from ammonia decomposition. Future work will focus on experimental validation of the optimized PSA cycles in pilot or full-scale systems to confirm their practical applicability and to refine the model under real operating conditions, including the effects of ammonia traces and their potential one-stage removal.

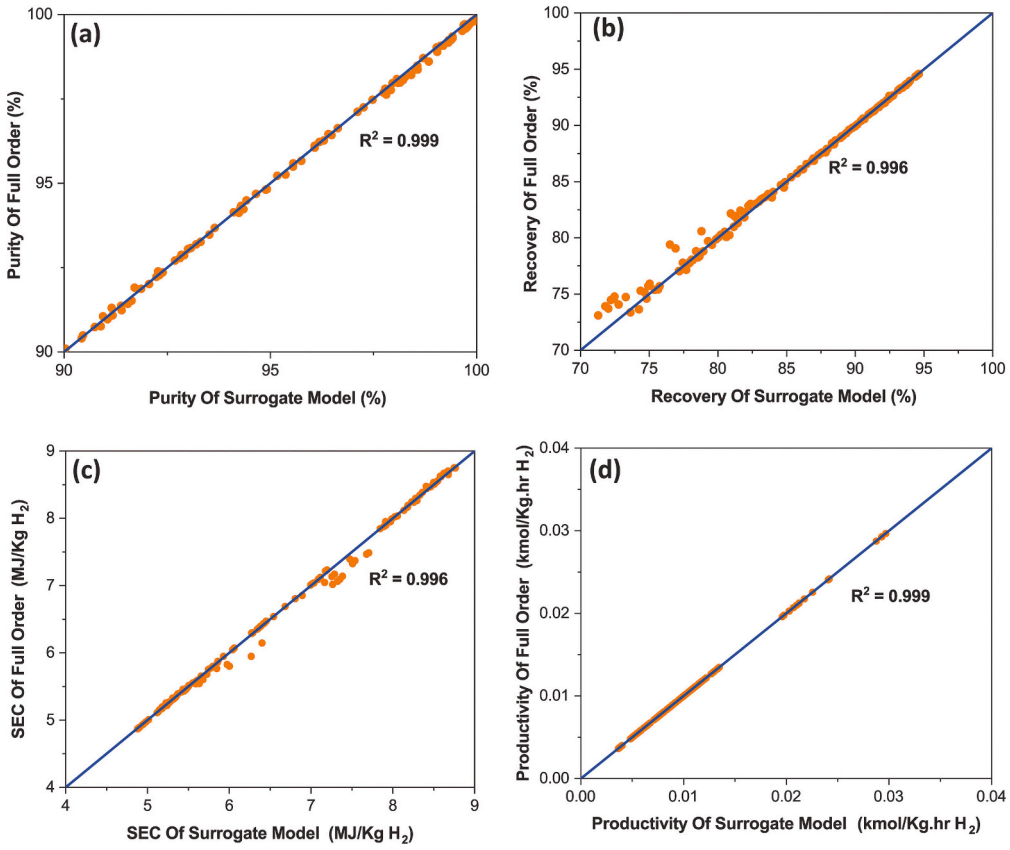

Fig. 13. Parity plots comparing full-order model predictions with surrogate model predictions.

CRediT authorship contribution statement

Bahare Abdoos: Writing – original draft, Visualization, Validation, Software, Methodology, Investigation, Formal analysis, Data curation, Conceptualization. **Almerinda Di Benedetto:** Writing – review & editing, Resources, Conceptualization. **Danilo Russo:** Writing – review & editing, Writing – original draft, Visualization, Supervision, Resources, Project administration, Methodology, Funding acquisition, Formal analysis, Conceptualization.

Declaration of competing interest

The authors declare that they have no known competing financial interests or personal relationships that could have appeared to influence the work reported in this paper.

Acknowledgements

This work was funded by the PRIN 2022 PNRR project "Ammonia-Based electrified processes integrated with fuel cell for power generation - AmBition" (P2022BEWCZ, CUP:E53D23017090001), in the framework of the European Union funding (NextGenerationEU), Ministero dell'Università e della Ricerca, Italiadomani Piano Nazionale di Ripresa e Resilienza.

Appendix A. Supplementary data

Supplementary data to this article can be found online at https://doi.org/10.1016/j.cej.2025.170994.

Data availability

Data will be made available on request.

References

[1] L. Tong, P. Bénard, Y. Zong, R. Chahine, K. Liu, J. Xiao, Artificial neural network based optimization of a six-step two-bed pressure swing adsorption system for hydrogen purification, Energy and AI 5 (2021), https://doi.org/10.1016/j.egyai.2021.100075.

[2] M. A. Habib, G. A. Q. Abdulrahman, A. B. S. Alquaity, and N. A. A. Qasem, "Hydrogen combustion, production, and applications: a review," Aug. 01, 2024, Elsevier B.V. doi: https://doi.org/10.1016/j.aej.2024.05.030, Alexandria Eng. J..

[3] N. Ma, W. Zhao, W. Wang, X. Li, and H. Zhou, "Large scale of green hydrogen storage: opportunities and challenges," Jan. 02, 2024, Elsevier Ltd. doi: https://doi.org/10.1016/j.ijhydene.2023.09.021, Int. J. Hydrog. Energy.

[4] T.E. Bell, L. Torrente-Murciano, H2 production via Ammonia decomposition using non-Noble metal catalysts: a review, Top. Catal. 59 (15–16) (2016) 1438–1457, https://doi.org/10.1007/s11244-016-0653-4.

[5] H.M.A. Hunter, et al., Demonstrating hydrogen production from ammonia using lithium imide – powering a small proton exchange membrane fuel cell, J. Power Sources 329 (2016) 138–147, https://doi.org/10.1016/j.jpowsour.2016.08.004.

[6] Y. Liu, M. Luo, W. Li, C. Zhou, X. Huo, Z. Pan, R. Chen, L. An, Techno-economic analysis of using ammonia as an energy carrier for renewable energy conversion and storage, Int. J. Hydrogen Energy 162 (2025) 150784, https://doi.org/10.1016/j.ijhydene.2025.150784.

[7] A. Bellucci Sessa, B. Abdoos, M. Turco, A. Di Benedetto, and D. Russo, "Ammonia-based processes integrated with fuel cells for electrical power generation: a review," Dec. 01, 2025, Elsevier Ltd. doi: https://doi.org/10.1016/j.rser.2025.116134, Renew. Sust. Energ. Rev..

[8] S.F. Yin, Q.H. Zhang, B.Q. Xu, W.X. Zhu, C.F. Ng, C.T. Au, Investigation on the catalysis of COx-free hydrogen generation from ammonia, J. Catal. 224 (2) (2004) 384–396, https://doi.org/10.1016/j.jcat.2004.03.008.

[9] M. Muhyuddin *et al.*, "Molybdenum disulfide as hydrogen evolution catalyst: from atomistic to materials structure and electrocatalytic performance," Dec. 01, 2023, Elsevier B.V. doi: https://doi.org/10.1016/j.jechem.2023.08.011, J. Energy Chem..

[10] M. Zhou, N. Li, D. Wang, S.S. Araya, V. Liso, Comparative analysis of degradation mechanisms in HT-PEM fuel cells under start–stop and load cycling with hydrogen and nitrogen-diluted feeds, Int. J. Hydrog. Energy 65 (2024) 639–647, https://doi.org/10.1016/j.ijhydene.2024.04.028.

[11] R. Augelletti, M. Conti, M.C. Annesini, Pressure swing adsorption for biogas upgrading. A new process configuration for the separation of biomethane and carbon dioxide, J. Clean. Prod. 140 (2017) 1390–1398, https://doi.org/10.1016/j.jclepro.2016.10.013.
[12] C.A. Grande, A.E. Rodrigues, Propane/propylene separation by pressure swing adsorption using zeolite 4A, Ind. Eng. Chem. Res. (2005), https://doi.org/10.1021/ie050671b.
[13] S. Sircar, "Pressure swing adsorption," Mar. 20, 2002, Am. Chem. Soc. doi: https://doi.org/10.1021/ie0109758, Ind. Eng. Chem. Res..
[14] S. Ahn, Y.W. You, D.G. Lee, K.H. Kim, M. Oh, C.H. Lee, Layered two- and four-bed PSA processes for H2 recovery from coal gas, Chem. Eng. Sci. 68 (1) (2012) 413–423, https://doi.org/10.1016/j.ces.2011.09.053.
[15] D.K. Moon, D.G. Lee, C.H. Lee, H2 pressure swing adsorption for high pressure syngas from an integrated gasification combined cycle with a carbon capture process, Appl. Energy 183 (2016) 760–774, https://doi.org/10.1016/j.apenergy.2016.09.038.
[16] A. Marcinek, P. Bárcia, J. Guderian, Scale-up analysis of a twin-bed PSA pilot plant, Adsorption 29 (3–4) (2023) 125–139, https://doi.org/10.1007/s10450-023-00382-2.
[17] L. Lin, Y. Tian, W. Su, Y. Luo, C. Chen, L. Jiang, Techno-economic analysis and comprehensive optimization of anon-sitehydrogen refuelling station system using ammonia: hybrid hydrogen purification with both high H2purity and high recovery, Sustain. Energy Fuels 4 (6) (2020) 3006–3017, https://doi.org/10.1039/c9se01111k.
[18] S. Ga, N. An, G.Y. Lee, C. Joo, J. Kim, Multidisciplinary high-throughput screening of metal–organic framework for ammonia-based green hydrogen production, Renew. Sust. Energ. Rev. 192 (2024), https://doi.org/10.1016/j.rser.2023.114275.
[19] A. Agarwal, L.T. Biegler, S.E. Zitney, Simulation and optimization of pressure swing adsorption systems using reduced-order modeling, Ind. Eng. Chem. Res. 48 (5) (2009) 2327–2343, https://doi.org/10.1021/ie071416p.
[20] J. Panerati, M. A. Schnellmann, C. Patience, G. Beltrame, and G. S. Patience, "Experimental methods in chemical engineering: Artificial neural networks–ANNs," Sep. 01, 2019, Wiley-Liss Inc. doi: https://doi.org/10.1002/cjce.23507, Can. J. Chem. Eng..
[21] K. Alkebsi, W. Du, Surrogate-assisted multi-objective particle swarm optimization for the operation of CO2 capture using VPSA, Energy 224 (2021), https://doi.org/10.1016/j.energy.2021.120078.
[22] F. Ye, S. Ma, L. Tong, J. Xiao, P. Bénard, R. Chahine, Artificial neural network based optimization for hydrogen purification performance of pressure swing adsorption, Int. J. Hydrog. Energy (2019) 5334–5344, https://doi.org/10.1016/j.ijhydene.2018.08.104.
[23] C.M. Rebello, I.B.R. Nogueira, Optimizing CO2 capture in pressure swing adsorption units: a deep neural network approach with optimality evaluation and operating maps for decision-making, Sep. Purif. Technol. 340 (2024), https://doi.org/10.1016/j.seppur.2024.126811.
[24] J. Du, et al., Development of hybrid surrogate model structures for design and optimization of CO2 capture processes: part I. Vacuum pressure swing adsorption in a confined space, Chem. Eng. Sci. 283 (2024), https://doi.org/10.1016/j.ces.2023.119379.
[25] M. Portarapillo, A. Bellucci Sessa, D. Russo, A. di Benedetto, Ammonia as a hydrogen carrier: energetic assessment of processes integrated with fuel cells for power generation, Energy Fuel (2025), https://doi.org/10.1021/acs.energyfuels.4c04626.
[26] S. Ga, N. An, G.Y. Lee, C. Joo, J. Kim, Multidisciplinary high-throughput screening of metal–organic framework for ammonia-based green hydrogen production, Renew. Sust. Energ. Rev. 192 (2024), https://doi.org/10.1016/j.rser.2023.114275.
[27] Z. Zhang, S. Liguori, T.F. Fuerst, J.D. Way, C.A. Wolden, Efficient Ammonia decomposition in a catalytic membrane reactor to enable hydrogen storage and utilization, ACS Sustain. Chem. Eng. 7 (6) (2019) 5975–5985, https://doi.org/10.1021/acssuschemeng.8b06065.
[28] J.G. Jee, M.B. Kim, C.H. Lee, Adsorption characteristics of hydrogen mixtures in a layered bed: binary, ternary, and five-component mixtures, Ind. Eng. Chem. Res. 40 (3) (2001) 868–878, https://doi.org/10.1021/ie0005046.
[29] A. Streb, M. Mazzotti, Adsorption for efficient low carbon hydrogen production: part 1—adsorption equilibrium and breakthrough studies for H2/CO2/CH4 on zeolite 13X, Adsorption 27 (4) (2021) 541–558, https://doi.org/10.1007/s10450-021-00306-y.
[30] B. Ghorbani, S. Zendehboudi, M. Bagheri, Z. Alizadeh Afrouzi, A. Lohi, A. Elkamel, Low-carbon hydrogen and methanol production via integrated vacuum swing adsorption, fuel cells, and carbon capture: exergy, economic, and optimization insights, Energy Fuel (2025), https://doi.org/10.1021/acs.energyfuels.5c00916.
[31] B. Wu, X. Zhang, Y. Xu, D. Bao, S. Zhang, Assessment of the energy consumption of the biogas upgrading process with pressure swing adsorption using novel adsorbents, J. Clean. Prod. 101 (2015) 251–261, https://doi.org/10.1016/j.jclepro.2015.03.082.
[32] M. Yáñez, F. Relvas, A. Ortiz, D. Gorri, A. Mendes, I. Ortiz, PSA purification of waste hydrogen from ammonia plants to fuel cell grade, Sep. Purif. Technol. 240 (2020), https://doi.org/10.1016/j.seppur.2019.116334.
[33] W. Kast, Adsorption Aus der Gasphase, VCH, Weinheim, 1988.
[34] H. Ahn, S.H. Hong, Y. Zhang, C.H. Lee, Experimental and simulation study on CO2 adsorption dynamics of a zeolite 13X column during blowdown and pressurization: implications of Scaleup on CO2 capture vacuum swing adsorption cycle, Ind. Eng. Chem. Res. 59 (13) (2020) 6053–6064, https://doi.org/10.1021/acs.iecr.9b05862.
[35] A. Marcinek, P. Bárcia, J. Guderian, Scale-up analysis of a twin-bed PSA pilot plant, Adsorption 29 (3–4) (2023) 125–139, https://doi.org/10.1007/s10450-023-00382-2.
[36] P. Kannan, P. Pal, F. Banat, Design of adsorption column for reclamation of methyldiethanolamine using homogeneous surface diffusion model, Oil & Gas Science and Technology – Revue d'IFP Energies nouvelles 75 (2020), https://doi.org/10.2516/ogst/2020073.
[37] Vassilis_Inglezakis,_Stavros_Poulopoulos_Adsorption,_Ion_Exchange, 2006. https://www.sciencedirect.com/book/monograph/9780444527837/adsorption-ion-exchange-and-catalysis.
[38] M. Bagheri, S. Fatemi, M. Fakhroleslam, A. Aleghafouri, Troubleshooting of an industrial ethane treatment unit: Ultradilute CO2 adsorption from ethane stream by a temperature swing adsorption process, Ind. Eng. Chem. Res. 63 (31) (2024) 13752–13761, https://doi.org/10.1021/acs.iecr.4c00807.
[39] M. Bagheri, S. Fatemi, M. Fakhroleslam, A. Aleghafouri, Troubleshooting of an industrial ethane treatment unit: Ultradilute CO2 adsorption from ethane stream by a temperature swing adsorption process, Ind. Eng. Chem. Res. 63 (31) (2024) 13752–13761, https://doi.org/10.1021/acs.iecr.4c00807.
[40] M. Bagheri, M. Fakhroleslam, S. Fatemi, Ultra-dilute CO2 capture in an ethane treatment plant via temperature swing adsorption: simulation-based analysis and multi-objective optimal design, Sep. Purif. Technol. 356 (2025), https://doi.org/10.1016/j.seppur.2024.129968.
[41] M.D. McKay, R.J. Beckman, W.J. Conover, A comparison of three methods for selecting values of input variables in the analysis of output from a computer code, Technometrics 42 (1) (2000) 55–61, https://doi.org/10.1080/00401706.2000.10485979.
[42] K.T. Leperi, D. Yancy-Caballero, R.Q. Snurr, F. You, 110th anniversary: surrogate models based on artificial neural networks to simulate and optimize pressure swing adsorption cycles for CO2 capture, Ind. Eng. Chem. Res. 58 (39) (2019) 18241–18252, https://doi.org/10.1021/acs.iecr.9b02383.
[43] J. Rother, T. Fieback, Multicomponent adsorption measurements on activated carbon, zeolite molecular sieve and metal-organic framework, Adsorption 19 (5) (2013) 1065–1074, https://doi.org/10.1007/s10450-013-9527-2.
[44] W.-G. Kim, J. Yang, S. Han, C. Cho, C.-H. Leer, H. Lee, Experimental and theoretical study on H_2/CO_2 separation by a five-step one-column PSA process, 1995.
[45] M. Yáñez, F. Relvas, A. Ortiz, D. Gorri, A. Mendes, I. Ortiz, PSA purification of waste hydrogen from ammonia plants to fuel cell grade, Sep. Purif. Technol. 240 (2020), https://doi.org/10.1016/j.seppur.2019.116334.
[46] F.I. Bashir, R.T.J. Porter, E. Catalanotti, H. Mahgerefteh, Performance and cost analysis of pressure swing adsorption for recovery of H2, CO, and CO2 from steelworks off-gases †, Energies (Basel) 18 (10) (2025) https://doi.org/10.3390/en18102440.